Skyrmion lattices in chiral metal–organic frameworks

Emma H. Wolpert[1], François-Xavier Coudert[2] & Andrew L. Goodwin[1]

[1]*Department of Chemistry, University of Oxford, Inorganic Chemistry Laboratory, South Parks Road, OX1 3QR, Oxford, UK*

[2]*PSL Research University, Chimie ParisTech–CNRS, Institut de Recherche de Chimie Paris, 75005 Paris, France*

Skyrmions are knot-like topologically-protected objects of use in data storage and low-energy smart devices. They can be generated by applying a magnetic field to certain chiral ferromagnets, with the knotted state involving a curling of the underlying magnetisation to give a nonzero winding number. Here we explore the possibility that chiral metal–organic frameworks (MOFs) might in principle host skyrmionic phases—realised not through the winding of magnetic spins but through that of guest molecule orientations. We propose a simple model for the interactions governing guest orientational order in chiral MOFs, with uniaxial strain acting as conjugate field. Using Monte Carlo simulations we show that this model gives a rich phase behaviour that includes molecular skyrmion crystals. *Ab initio* molecular dynamics simulations carried out for a candidate chiral MOF of tractable complexity demonstrate that our simple model effectively captures its underlying energetics. Our results suggest that skyrmionic states may indeed be realisable in MOFs and related porous media and may even arise spontaneously in thin-film samples.

Topologically-protected objects such as skyrmions,[1] merons,[2] and hopfions[3] are natural candidates for device applications because the information contained in their topological charge is preserved indefinitely in the absence of external perturbations.[4,5] An important experimental realisation is the skyrmion crystal phase of some chiral ferromagnets,[6–8] of which MnSi is probably the most famous.[9,10] Here the local magnetisation generated by Heisenberg ferromagnetism has essentially uniform magnitude, but the antisymmetric Dzyalonshinskii-Moriya (D-M) interaction promotes a curling of the magnetisation field. For the right balance of temperature and external field this curling collapses into a lattice of skyrmion cores whose magnetisation opposes that of the bulk and of the applied field [Fig. 1(a)]. Similar vortex-like defects feature strongly in the physics of nematic liquid crystals [Fig. 1(b)],[11–13] and these are rigorously skyrmionic and thermodynamically stable for model systems with chiral interactions when placed under confinement.[14] Yet the number of different chemical families known experimentally to support skyrmionic textures remains remarkably small, due in no small part to the difficulty of engineering the antisymmetric interactions at the heart of skyrmion physics.[15,16] In the case of MnSi, for example, the nonvanishing D-M interaction relies on the peculiar combination of spin–orbit coupling and chirality of its B20 lattice type.[10] Consequently, there is strong interest in realising new skyrmionic phases and, more broadly, diversifying the chemical space accessible for topological materials design.

Whereas chirality is rare amongst ferromagnetic metals, it is commonplace amongst metal–organic frameworks (MOFs).[17–19] MOFs are porous coordination-network solids assembled from inorganic nodes and organic linkers; by varying the chemistry and connectivity of each component it is possible to control the topology and dimensions of the resulting three-dimensional network.[20–23] Coordination polymers and hybrid frameworks are related systems,[24,25] and for simplicity we use include these families here under the umbrella of the term ‘MOF’. There are now a number of well-established strategies for synthesising chiral MOFs, including many that use only achiral reagents,[26] or involve only host–guest interactions, such as adsorption of achiral molecules.[27] Combining Mn^{2+} ions and sodium formate, for example, generates the phase $Na[Mn(HCOO)_3]$, the anionic manganese–formate framework of which shares the same chiral B20 architecture of MnSi [Fig. 1(c)].[28] Like many MOFs, this material is weakly antiferromag-

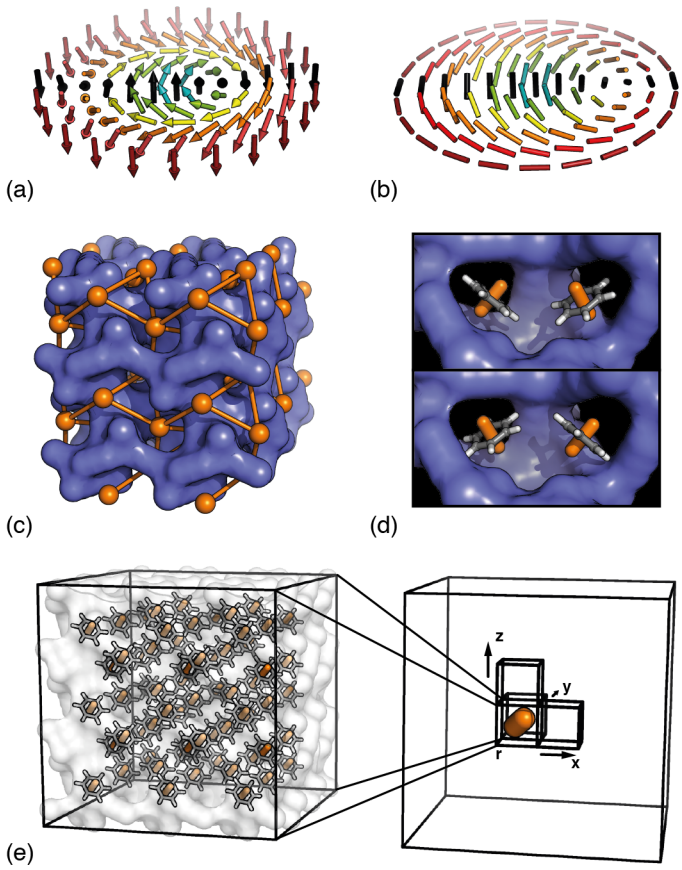

Figure 1: **Skyrmions and their relevance to MOFs.** (a) A magnetic skyrmion is a topological object involving winding of the local magnetisation (shown here as arrows, coloured according to orientation). Note the path coloured black involves a rotation of the magnetisation by 360°. (b) Nematic liquid crystals show similar states, except that winding by 180° is now possible because nematic directors are unchanged under inversion. (c) The network of Na sites (coloured orange) in the MOF-like system $NaMn(HCOO)_3$ adopts the same chiral lattice as that of Mn atoms in the magnetic skrymion phase MnSi. (d) In guest-loaded chiral MOFs the interactions between neighbouring guest molecules involve both symmetric and antisymmetric components—which are key in stabilising skyrmions. For example, if the orientations of two benzene molecules in a chiral pore are interchanged then the average interaction energy reflects the symmetric component and the difference in energy reflects the antisymmetric component. (e) Our coarse graining involves mapping the average orientation of guest molecules within a finite volume onto a single nematic degree of freedom (orange bar on right). Hence any topological textures that emerge in our coarse grained simulations involve lengthscales that are orders of magnitude greater than the distances between neighbouring guest molecules.

netic with no strong spin-orbit coupling, and hence is unlikely to support a magnetic skyrmion phase.[29,30] But while magnetic interactions in MOFs are notoriously weak, the effective interactions between molecules contained within their pores can be strong indeed—such is the basis, after all, of the 'crystalline sponge' concept[31,32] and the origin of orientational order/disorder transitions in *e.g.* hybrid perovskites.[33–37] Moreover, the pore networks of chiral MOFs are of course themselves chiral,[17] and so the interactions between guest molecule confined within these pores automatically include an antisymmetric component [Fig. 1(d)]. So guest-loaded chiral MOFs are perhaps surprisingly well placed to support topologically nontrivial states, built on collective orientational degrees of freedom—rather than the more usual magnetic order. We therefore pose the question: might MOFs be capable, in principle, of harbouring orientational skyrmions?

Here we proceed to answer this question in three stages. First, we establish a simple interaction model that relates the problem of orientational order in MOFs to that of magnetic order in systems such as MnSi, on the one hand, and also to that of orientational order in chiral nematic liquid crystals, on the other hand. Second, we perform a series of classical Monte Carlo simulations in order to establish the phase behaviour to which our model gives rise. In this way we identify a number of accessible topologically nontrivial phases, including that of a skyrmion crystal. And, third, we use *ab initio* molecular dynamics (AIMD) simulations to establish the relevance of our simple microscopic model to the thermodynamic behaviour of a representative chiral MOF. We argue on this basis that MOFs are viable hosts for emergent topological objects, and we conclude by discussing some of the challenges and opportunities associated with realising, characterising, and exploiting skyrmionic MOFs.

Results

Interaction model. We consider here a model where guest molecules are confined within a MOF pore network, and the relevant microscopic degrees of freedom are the orientations of individual molecules whose position is fixed in the host lattice. The most general descriptions of these orientations involve unit quaternions or rotation matrices, but we focus instead on the simpler represen-

tation offered by quadrupoles because of (i) the particular relevance to commonly-encountered rodlike (*e.g.* methylammonium) or planar (*e.g.* guanidinium, imidazolium) molecules, (ii) the straightforward mapping to director degrees of freedom in nematic liquid crystals, and (iii) the direct coupling to uniaxial strain, itself expressible as a rank-2 tensor.[38,39] Explicitly, we denote the orientation of molecule i parallel (if rodlike) or normal (if planar) to an axis $\mathbf{s}_i = \pm(s_{ix}, s_{iy}, s_{iz})$ by the symmeric tensor

$$\mathbf{Q}_i = \begin{bmatrix} s_{ix}^2 & s_{ix}s_{iy} & s_{ix}s_{iz} \\ s_{iy}s_{ix} & s_{iy}^2 & s_{iy}s_{iz} \\ s_{iz}s_{ix} & s_{iz}s_{iy} & s_{iz}^2 \end{bmatrix}. \tag{1}$$

By analogy to the microscopic Hamiltonian of relevance to *e.g.* MnSi—which contains symmetric exchange, antisymmetric exchange (D-M), and Zeeman terms[10,16,40,41]—we form the Hamiltonian

$$\hat{\mathcal{H}} = -\hat{J}\sum_{ij}\mathbf{Q}_i : \mathbf{Q}_j - \hat{K}\sum_{ij}(\mathbf{Q}_i \star \mathbf{Q}_j)\cdot\mathbf{r}_{ij} + \hat{A}\mathbf{E} : \sum_i \mathbf{Q}_i. \tag{2}$$

Here $\mathbf{Q}_i : \mathbf{Q}_j = \mathrm{Tr}(\mathbf{Q}_i\mathbf{Q}_j^{\mathrm{T}}) = (\mathbf{s}_i\cdot\mathbf{s}_j)^2$ is the (symmetric) scalar product of two tensors, $\mathbf{Q}_i\star\mathbf{Q}_j = (\mathbf{s}_i\cdot\mathbf{s}_j)(\mathbf{s}_i\times\mathbf{s}_j)$ is the (antisymmetric) vector product, the vector $\mathbf{r}_{ij}$ connects neighbouring sites i, j, and

$$\mathbf{E} = \begin{bmatrix} +\frac{\epsilon}{2} & 0 & 0 \\ 0 & +\frac{\epsilon}{2} & 0 \\ 0 & 0 & -\epsilon \end{bmatrix} \tag{3}$$

is the uniaxial volume-conserving strain tensor oriented along an arbitrary crystal axis (here, $\mathbf{c}$). The underlying lattice will be dictated by the topology of the MOF pore network, which we assume to be chiral. The coefficients $\hat{J}$ and $\hat{K}$ capture the strengths of symmetric and antisymmetric 'exchange', and $\hat{A}$ reflects the coupling of molecular orientations to strain (we will come to show it behaves as an effective elastic constant). We use the 'hat' representation to distinguish these microscopic parameters from their continuous analogues, given in due course below.

To convey the qualitative meaning of this interaction model in the context of a guest-filled MOF, we consider the pair of scenarios sketched in Fig. 1(d). In a chiral pore network, the inter-

actions between molecules depend on their mutual orientation. The symmetric 'exchange' term of strength $\hat{J}$ reflects the general tendency for neighbouring molecules to align with one another, and clearly is unaffected by interchanging molecular orientations. So this symmetric contribution would have the same value for both scenarios in Fig. 1(d). But we know that the two scenarios are chemically different due to the chiral host framework, and this difference is captured by the antisymmetric term of strength $\hat{K}$. If the chirality of a MOF pore network strongly influences the interactions between guest species then $\hat{K}$ will be large—perhaps as large as, or larger than, $\hat{J}$—and neighbouring molecules will tend to rotate in a specific direction dictated by the lattice handedness. This will emerge as a key driving force for skyrmion formation. Finally, the elastic term captures straightforwardly the alignment of guest orientations in response to an external strain field: *e.g.* for planar molecules to align normal to the axis along which a crystal is compressed. This term captures the symmetry-breaking influence of the strain, and can stabilise skyrmion cores lying parallel to the strain axis.

Because skyrmions emerge on a lengthscale fundamentally removed from that of the underlying microscopic interactions, the convention is to coarse-grain to the corresponding continuum Hamiltonian:[16,42]

$$\begin{aligned}\mathcal{H} &= -J\sum_{\mathbf{r}}\mathbf{Q}_{\mathbf{r}} : (\mathbf{Q}_{\mathbf{r}+\mathbf{x}} + \mathbf{Q}_{\mathbf{r}+\mathbf{y}} + \mathbf{Q}_{\mathbf{r}+\mathbf{z}}) \\ &\quad -K\sum_{\mathbf{r}}\left[(\mathbf{Q}_{\mathbf{r}} \star \mathbf{Q}_{\mathbf{r}+\mathbf{x}})\cdot\mathbf{x} + (\mathbf{Q}_{\mathbf{r}} \star \mathbf{Q}_{\mathbf{r}+\mathbf{y}})\cdot\mathbf{y} + (\mathbf{Q}_{\mathbf{r}} \star \mathbf{Q}_{\mathbf{r}+\mathbf{z}})\cdot\mathbf{z}\right] \\ &\quad +A\mathbf{E} : \sum_{\mathbf{r}}\mathbf{Q}_{\mathbf{r}}, \end{aligned} \tag{4}$$

where the quadrupolar degrees of freedom $\mathbf{Q}_{\mathbf{r}}$ now represent the average molecular alignment director for a finite volume element centred at position $\mathbf{r}$, and $\mathbf{x}, \mathbf{y}, \mathbf{z}$ are unit vectors joining neighbouring volume elements along each cartesian axis [Fig. 1(e)]. The values of J, K, A are directly proportional to $\hat{J}, \hat{K}, \hat{A}$.

We note that our model is closely related to that developed in Ref. 14 to describe a particular class of chiral nematic liquid crystals, but with two important distinctions. The first is in micro-

scopic detail: the quadrupolar degrees of freedom in our model occupy well-defined sites, and so we are not integrating out translational degrees of freedom. And, second, the antisymmetric contribution to the liquid crystal Hamiltonian is introduced by a three-body interaction, which may be difficult to realise and/or control experimentally; in our model this term is pairwise (as for the D-M interaction) and arises naturally from the chirality of the underlying lattice.

Phase behaviour. We proceeded to determine the phase behaviour captured by our Hamiltonian (4), using classical Monte Carlo simulations to produce representative configurations as a function of strain, temperature, and balance of antisymmetric and symmetric exchange terms. On the basis of the corresponding small-angle scattering patterns (see Methods for details) we identified six distinct phases, the stability fields for which are shown on the phase diagram in Fig. 2(a). We obtained equivalent phase diagrams when preparing configurations at fixed $J, K, A\epsilon$ and slowly varying T, on the one hand, and at fixed J, K, T with slowly varying $A\epsilon$ on the other hand.[16] In neither case did we observe any significant complexity with temperature, and so the key results can be explained in terms of the two-dimensional phase map projected into $A' = A\epsilon/J, K' = K/J$ space [inset to Fig. 2(a)].

At high strains or low K' the system is ferroquadrupolar (FQ), by which we mean that there is collective alignment of all molecular orientations along the same direction in which strain is applied (tensile for rod-like molecules; compressive for planar molecules); all that varies is the corresponding order parameter. Below a critical line in A', K'-space the phase behaviour is dominated by helical states where the quadrupole orientation lies normal to, and precesses around, either a single propagation vector $\mathbf{k} \in \langle 100 \rangle^*$ (H), $\langle 110 \rangle^*$ (H′) or a pair of propagation vectors $\mathbf{k}_1, \mathbf{k}_2 \in \langle 210 \rangle^*$ that alternate along $[001]$ (H*) [Fig. 2(b)]. These helical states are closely related to those found in a variety of chiral magnets.[43,44]

Our key result is that specific combinations of A' (relatively low strains) and K' (moderate to strong antisymmetric exchange) stabilise two topologically nontrivial states containing skyrmions [Fig. 2(c)]. Both are skyrmion crystals, but they differ in terms of the skyrmion density: the 'SkX'

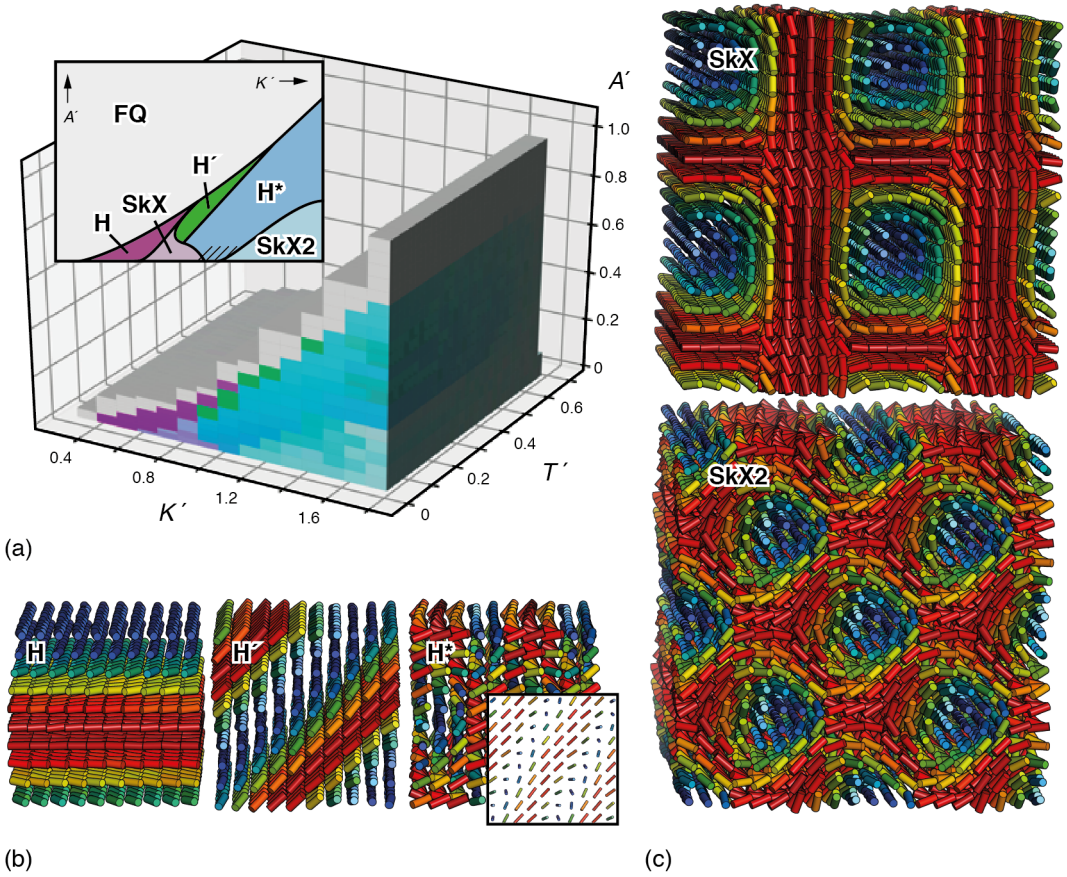

Figure 2: **Emergent phase diagram from Monte Carlo simulations.** (a) Phase stability as a function of relative antisymmetric interaction strength (K'), applied strain (A') and simulation temperature (T'); different phases are identified and coloured on the basis of their small-angle scattering patterns (see Methods). Since the dependence on T' is uninteresting, we summarise the phase behaviour by projecting onto A', K'-space (inset). The dominant phase at high strains is the trivial ferroquadrupolar (FQ) state. At low strains there is a series of helical (H, H′, H*) and skrymionic (SkX, SkX2) phases. (b) Orientational order in the helical phases involves precession of the nematic alignment axis around one (H, H′) or two (H*) directions; a slice through the latter configuration is shown in the inset. (C) The two skyrmion crystal phases we observe possess the same basic structure but differ in terms of skyrmion density. Here we have shown a $2 \times 2 \times 2$ supercell of our simulation cell in order to highlight the emergent square lattice in each case.

phase contains one skyrmion core in our simulation box, and the 'SkX2' crystal contains two. We expect the distinction may be an artefact of the finite simulation box size. Larger simulations may show a continuous evolution of skyrmion density and accommodate other lattice geometries, such as the triangular packing observed for magnetic skyrmions.

What do these phases mean in terms of the orientations of guest molecules within the corresponding MOF pore networks? On a local level—*e.g.* on the order of perhaps a few unit cells—all guest molecules are aligned along a common axis, as if in a ferroquadrupolar arrangement. But on a longer lengthscale (10–100 nm for magnetic skyrmions) this alignment axis curls around the skyrmion core, creating a topological defect at its centre. That defect can move through thermal fluctuations in molecular orientations, but is topologically protected and cannot be removed. So for specific values of A' and K', any system whose behaviour is governed by Eq. (4) can in principle exhibit a skyrmion phase under appropriate conditions. What remains for us to show is that Eqs. (2) and (4) can apply to suitably-chosen MOF systems.

Molecular dynamics simulations. The typical lengthscale associated with skyrmionic textures (10–100+ nm) is much too large for explicit atomistic simulation using *ab initio* methods. Thus the final stage of our approach is to perform AIMD simulations performed across a range of temperatures and uniaxial strains to establish whether the thermodynamic behaviour of a suitable MOF might be described in terms of guest molecule interactions of the form given in Eq. (2). In the absence of a MOF known experimentally to support skyrmions, we chose to study a model system that at once captures the key flavours of our anticipated design rules—namely, quadrupolar hosts embedded within a chiral framework—whilst also allowing AIMD simulations to be computationally tractable (small unit cell, high symmetry, closed-shell configuration). For these reasons we have focussed on the hypothetical, but chemically sensible, analogue of $Na[Mn(HCOO)_3]$ in which the open-shell Mn^{2+} ion is replaced by closed-shell Al^{3+}, the formate linker replaced by the slightly-extended azide anion (N_3^-) to open up the pore network,[45] and the guest Na^+ ions replaced by (planar) benzene molecules that now fit in the larger pores. Hence our model system has formula $[Al(N_3)_3]\cdot C_6H_6$ and is characterised by the same chiral space-group symmetry ($P2_13$)

as Na[Mn(HCOO)$_3$] and MnSi. Relaxation of the structure using density function theory (DFT) calculations showed the system to be energetically and mechanically stable [Fig. 3(a)], including under application of uniaxial strain along $\pm[001]$. Full details of the relaxed structure are given in the Supporting Information.

Our AIMD simulations were carried out for a range of temperatures 10–300 K and uniaxial strains 0–7% using a single $P2_13$ [Al(N$_3$)$_3$]·C$_6$H$_6$ unit cell (containing four formula units) with periodic boundary conditions applied. By inspection we confirm that benzene orientations fluctuate more strongly at higher temperatures (as expected) and align progressively more strongly along the strain axis as strain was increased. We analysed post-equilibrium configurations using moment of inertia tensors to identify quadrupole orientations for each of the four benzene molecules in the simulation cell. This allowed us to calculate the corresponding $\sum_{ij} \mathbf{Q}_i : \mathbf{Q}_j$, $\sum_{ij} \mathbf{Q}_i \star \mathbf{Q}_j$ and $\mathbf{E} : \sum_i \mathbf{Q}_i$ terms, and in due course determine a coarse-grained configurational energy of the form $E_{\mathrm{CG}} = E_0 - \hat{J} \sum_{ij} \mathbf{Q}_i : \mathbf{Q}_j - \hat{K} \sum_{ij} \mathbf{Q}_i \star \mathbf{Q}_j + \hat{A}\mathbf{E} : \sum_i \mathbf{Q}_i$. Here the (anti)symmetric exchange coefficients include not only direct interactions between the C$_6$H$_6$ molecules (perhaps relatively unimportant) but also the effective interactions as mediated by the surrounding [Al(N$_3$)$_3$] framework. Likewise the strain term subsumes within it the usual elastic strain energy since $\mathbf{E} : \sum_i \mathbf{Q}_i \propto \epsilon^2$.

Taking our ensemble of AIMD configurations we then used a linear least squares minimisation to identify the values of $E_0, \hat{J}, \hat{K}, \hat{A}$ corresponding to the [Al(N$_3$)$_3$]·C$_6$H$_6$ system, that optimised the goodness-of-fit

$$\chi^2 = \sum_{T,\epsilon} \left[\frac{\langle E_{\mathrm{AIMD}} \rangle(T,\epsilon) - \langle E_{\mathrm{CG}} \rangle(T,\epsilon)}{\sigma(T,\epsilon)} \right]^2 , \tag{5}$$

where the averages are taken over all equilibrium configurations at constant T, ϵ, and the uncertainty σ is given by the corresponding standard deviation in energy. The match between E_{AIMD} and E_{CG} values, as shown in Fig. 3(b), is remarkable given that our coarse graining maps the $3N - 3 = 261$ positional degrees of freedom of the AIMD simulations onto just eight (the orientations of each of four quadrupoles). The implication is that the low-energy phonons are dominated

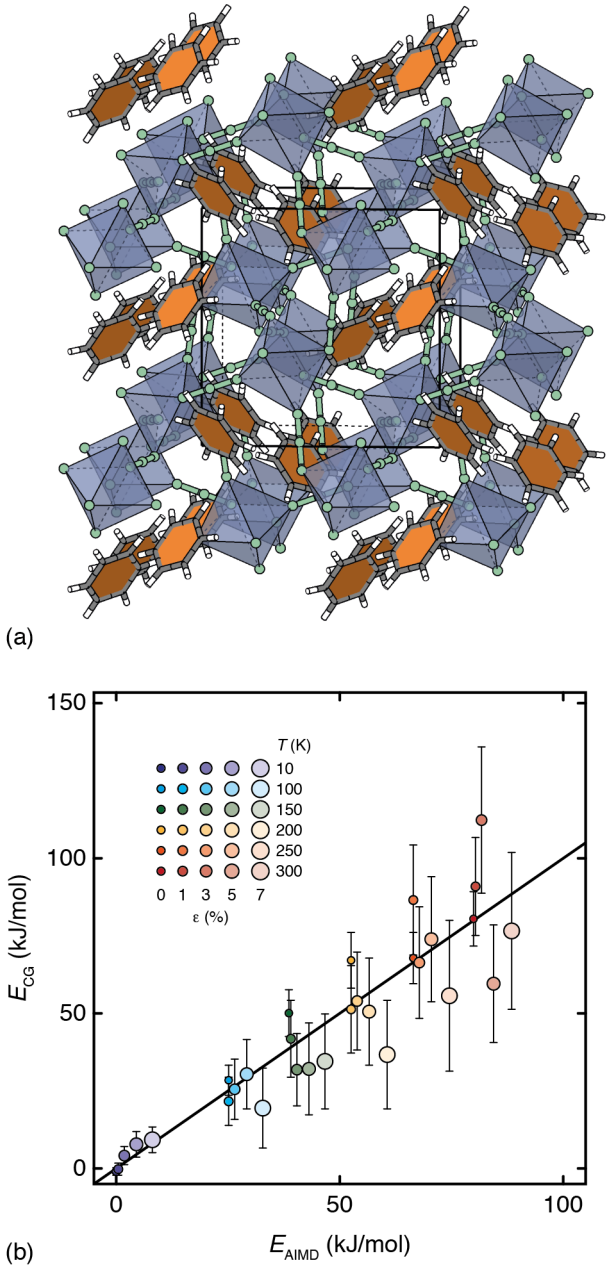

Figure 3: **Ab initio molecular dynamics simulations of a MOF skyrmion candidate.** (a) Representation of the relaxed structure of $Al(N_3)_3{\cdot}C_6H_6$ determined using DFT. Al coordination polyhedra shown in blue, azide links in green, and benzene molecules in grey, white and orange. The centres of the guest molecules occupy the same network of positions shown in Fig. 1(c). (b) Match between coarse-grained and AIMD configurational energies as a function of simulation temperature (symbol colour) and applied strain (symbol size). The solid line shows the relation $E_{\rm CG} = E_{\rm AIMD}$. That our data cluster around this line reflects the ability of the coarse grained Hamiltonian Eq. (2) to capture the key thermodynamics of this representative phase at low temperatures and small applied strains. Our key result is that this same Hamiltonian is capable of stabilising skyrmion crystal phases, as shown in Fig. 2(c).

by benzene rotations and modes that couple strongly to these rotations. Hence we conclude that the Hamiltonian (2)—which we have shown can support skyrmionic phases—is a good first-order representation of thermodynamic behaviour of this model MOF system. Moreover, that $\hat{K}$ is finite implies that the chirality of the host framework does impose a nontrivial antisymmetric coupling between neighbouring guests, as envisaged in Fig. 1(d).

Discussion

From the above models, both microscopic and coarse-grained, we show that MOF skyrmion phases may indeed be possible. Where should we look to find one experimentally? Sadly our proof-of-concept model system $[Al(N_3)_3]\cdot C_6H_6$ is likely not the right place, were it ever to be made: our AIMD simulations show $\hat{J}$ to be positive in this case, which stabilises antiferroquadrupolar order and locates the phase outside of the various stability fields shown in Fig. 2(b). But the balance between ferro- and antiferro-quadrupolar order in some MOFs can be switched by as simple a means as varying ionic radius—*e.g.* as in $[C(NH_2)_3][M(HCOO)_3]$ (M = Cd *vs* Mn)[46]—so variants on the theme may well be worthwhile avenues for exploration. There is certainly vast scope for exploiting the chemical and topological versatility of the family (and indeed that of other classes of porous materials, including COFs[47] and zeolites[48,49]). But we anticipate systematics will be crucial. For example, in some achiral MOFs, such as the imidazolium cyanoelpasolites, framework size can vary smoothly the magnitude of symmetric quadrupolar exchange;[39] one anticipates that similar strategies may allow optimisation of $K' = K/J$ in chiral systems. And, since uniaxial strain can be applied and controlled directly to single-crystal samples,[50] it may not be too difficult to navigate much of K', A' space using a handful of judiciously chosen MOF compositions. It may even prove possible to access appropriate strains epitaxially in thin-film samples.[51]

Just as for the characterisation of magnetic skyrmions, small-angle scattering (now either X-ray or neutron) will be sensitive to the formation of ordered orientational skyrmion phases, and we expect this to be the most straightforward method for evidencing their existence. Direct observation may also be possible by exploiting *e.g.* spatially resolved X-ray birefringence imaging.[52,53]

If MOF skyrmion crystals with emergent periodicities commensurate with those of visible light prove accessible, one should observe optical Bragg scattering from the lattice—as in many liquid crystalline phases.[54] In such cases a colour change is direct experimental evidence of skyrmion crystal formation and may form the basis for efficient chemical, temperature, or pressure sensors. Any application to data storage will require solving the (very) tricky problem of direct manipulation of individual skyrmions—a challenge also faced historically in the case of the magnetic systems.[5] From a theory perspective, the phenomenological model at the heart of our study may prove too simplistic for many systems: we have not taken into account any single-site anisotropy, for example (*cf* the importance of induced anisotropy in MnSi/Si(111) thin films[55,56]); nor have we included any long-range terms, such as dipolar interactions. There is plenty of scope for further refinement in this regard. Nevertheless the primary aim of our study has simply been to motivate the search for mesoscopic topological textures in a broad class of materials not normally associated with emergent phenomena.

Methods

Monte Carlo simulations A custom Monte Carlo (MC) code was used to generate a statistical sampling of quadrupole orientations of a coarse grained chiral MOF with quadrupolar guests. Simulations were performed using a $10 \times 10 \times 10$ supercell of the simple cubic lattice with one quadrupole per lattice point (*i.e.* 1000 quadrupoles per configuration) and with periodic boundary conditions applied. The Monte Carlo energy was calculated according to Eq. (4), modified to include second-nearest neighbour terms to give a better approximation of the continuum field theory as discussed in Ref. 42:

$$\mathcal{H}_{\mathrm{MC}} = \mathcal{H} + \mathcal{H}_2, \tag{6}$$

where

$$\begin{aligned} \mathcal{H}_2 &= J_2 \sum_{\mathbf{r}} \mathbf{Q_r} : (\mathbf{Q_{r+2x}} + \mathbf{Q_{r+2y}} + \mathbf{Q_{r+2z}}) \\ &\quad + K_2 \sum_{\mathbf{r}} \left[(\mathbf{Q_r} \star \mathbf{Q_{r+2x}}) \cdot \mathbf{x} + (\mathbf{Q_r} \star \mathbf{Q_{r+2y}}) \cdot \mathbf{y} + (\mathbf{Q_r} \star \mathbf{Q_{r+2z}}) \cdot \mathbf{z} \right], \end{aligned} \tag{7}$$

with $J_2 = J/16, K_2 = K/8$. Simulations were started at high temperatures and cooled slowly ($T_{i+1} = T_i - 0.02J$) for constant K' and A' sampled from a suitably-chosen grid. Each MC move involved a random reorientation of a randomly-chosen quadrupole, and was accepted or rejected according to the standard Metropolis criterion.[57] The number of MC steps required to reach equilibration was determined by the autocorrelation function. At each temperature point the simulation proceeded for ten times as many steps again, and results were taken as the average over five independent post-equilibrium configurations. At very low temperatures and very high strains equilibration became difficult, and configurations were collected after a suitably large number of accepted moves. By analogy to the test performed in Ref. 42 we also carried out MC simulations at constant K', T with varying A' but equilibration was substantially more difficult in this case.

Phase diagram determination Phase identification was automated by analysing small-angle scattering patterns generated from the MC simulations. Atomistic representations of the MC configurations were prepared by replacing each quadrupole by a set of five identical scattering objects equally displaced from the quadrupole position along both directions of the quadrupole axis. The

small-angle scattering function $I(\mathbf{q})$ was generated by Fourier transform of the resulting scattering density. This function was then reduced to three two-dimensional scattering cuts perpendicular to each of the crystal axes that were subsequently averaged over the first Brillouin zone (BZ) and normalised: for example,

$$I_{\mathbf{a}}(\mathbf{k}) = \alpha \sum_{\mathbf{G}} I(\mathbf{G} + \mathbf{k}), \tag{8}$$

where $\mathbf{G}$ is a reciprocal lattice vector ($\in \{(0, -1, -1)^*, \ldots, (0, 1, 1)^*\}$) lying in the relevant plane of reciprocal space, α is a scaling factor chosen such that $\max(I_{\mathbf{a}}) = 1$, and $\mathbf{k} \perp \mathbf{a}$ is a scattering vector contained within the first BZ. The functions $I_{\mathbf{b}}(\mathbf{k})$ and $I_{\mathbf{c}}(\mathbf{k})$ were defined analogously. Note that BZ averaging removes the quadrupole scattering-object form factor,[58] and hence these scattering functions are invariant with respect to the displacement magnitude used to generate the real-space configurations. The scattering in each cut was interpreted in terms of its on-axis ($\mathbf{k} \perp \mathbf{a}, \mathbf{b}$ or $\mathbf{c}$) and off-axis components. The strengths and anisotropy of these components were used to derive the numeric RGB values that then colour the corresponding voxel in the phase diagram of Fig. 2(a). The explicit formulae involved are given as SI.

Quantum mechanical calculations. Quantum chemical calculations were performed to confirm the stability and monitor the behaviour of $[Al(N_3)_3]\cdot C_6H_6$ under strain. Density Functional Theory (DFT) calculations were used first to optimise the materials geometry, and then calculate its elastic properties at zero temperature. All calculations were performed using the CRYSTAL14 software.[59] We used the Perdew, Burke, and Ernzerhof (PBE) exchange–correlation functional[60] with double-ζ plus polarization basis sets for all atoms. The shrinking factor of the reciprocal space net was set to 3. A representative input file that includes all relevant control parameters, together with the crystallographic details of the relaxed structure are provided as SI.

***Ab initio* molecular dynamics (AIMD) simulations** The behaviour of the $[Al(N_3)_3]\cdot C_6H_6$ framework as a function of temperature and strain was studied by means of density functional theory (DFT) based molecular dynamics (MD) simulations with the CP2K software package.[61] Starting from the geometry-optimised structure, we carried out AIMD simulations by employing the hybrid Gaussian and plan-wave method GPW as implemented in the Quickstep module in CP2K. Again,

the PBE exchange–correlation functional[60] was used, along with DZVP-GTH-PADE basis sets. The simulations were performed in the constant-volume (N, V, T) ensemble with fixed size and shape of the unit cell, and with periodic boundary conditions. A timestep of 0.5 fs was used, and the AIMD simulations consisted of an equilibration period of 10 ps to determine the energy as a function of temperature and strain. We chose the plane-wave cut-off for the electronic density to be 750 Ry and a relative cut-off of 60 Ry for high accuracy, after checking that the energy converged at these values. A representative input file is provided as SI.

1. Skryme, T. H. A non-linear field theory. *Proc. R. Soc. Lond. A* **260**, 127–138 (1961).

2. Yu, X. Z. *et al.* Transformation between meron and skyrmion topological spin textures in a chiral magnet. *Nature* **564**, 95–98 (2018).

3. Borisov, A. B. & Rybakov, F. N. Dynamical toroidal hopfions in a ferromagnet with easy-axis anisotropy. *JETP Lett.* **90**, 544–547 (2009).

4. Jonietz, F. *et al.* Spin transfer torques in MnSi at ultralow current densities. *Science* **330**, 1648–1651 (2010).

5. Romming, N. *et al.* Writing and deleting single magnetic skyrmions. *Science* **341**, 636–639 (2013).

6. Seki, S., Yu, X. Z., Ishiwata, S. & Tokura, Y. Observations of skyrmions in a multiferroic material. *Science* **336**, 198–201 (2012).

7. Huang, S. X. & Chien, C. L. Extended skyrmion phase in epitaxial FeGe(111) thin films. *Phys. Rev. Lett.* **108**, 267201 (2012).

8. Nagaosa, N. & Tokura, Y. Topological properties and dynamics of magnetic skyrmions. *Nat. Nanotech.* **8**, 899–911 (2013).

9. Pappas, C. *et al.* Chiral paramagnetic skyrmion-like phase in MnSi. *Phys. Rev. Lett.* **102**, 197202 (2009).

10. Mühlbauer, S. *et al.* Skyrmion lattice in a chiral magnet. *Science* **323**, 915 (2009).

11. Leonov, A. O., Dragunov, I. E., Rößler, U. K. & Bogdanov, A. N. Theory of skyrmion states in liquid crystals. *Phys. Rev. E* **90**, 042502 (2014).

12. Ackerman, P. J., Trivedi, R. P., Senyuk, B., van de Lagemaat, J. & Smalyukh, I. I. Two-dimensional skyrmions and other solitonic structures in confinement-frustrated chiral nematics. *Phys. Rev. E* **90**, 012505 (2014).

13. Cattaneo, L. *et al.* Electric field generation of skyrmion-like structures in a nematic liquid crystal. *Soft Matter* **12**, 853–858 (2016).

14. Fukuda, J.-I. & Žumer, S. Quasi-two-dimensional Skyrmion lattices in a chiral nematic liquid crystal. *Nat. Commun.* **2**, 246 (2011).

15. Rößler, U. K., Bogdanov, A. N. & Pfleiderer, C. Spontaneous skyrmion ground states in magnetic metals. *Nature* **442**, 797–801 (2006).

16. Yi, S. D., Onoda, S., Nagaosa, N. & Han, J. H. Skyrmions and anomalous Hall effect in a Dzyaloshinskii-Moriya spiral magnet. *Phys. Rev. B* **80**, 054416 (2009).

17. Kepert, C. J. & Rosseinsky, M. J. A porous chiral framework of coordinated 1,3,5-benzenetricarboxylate: quadruple interpenetration of the (10,3)-a network. *Chem Commun.* 31–32 (1998).

18. Han, Z., Shi, W. & Cheng, P. Synthetic strategies for chiral metal-organic frameworks. *Chinese Chem. Lett.* **29**, 819–822 (2018).

19. Ma, L., Abney, C. & Lin, W. Enantioselective catalysis with homochiral metal–organic frameworks. *Chem. Soc. Rev.* **38**, 1248–1256 (2009).

20. Hoskins, B. F. & Robson, R. Design and construction of a new class of scaffolding-like materials comprising infinite polymeric frameworks of 3D-linked molecular rods. A reappraisal of the $Zn(CN)_2$ and $Cd(CN)_2$ structures and the synthesis and structure of the diamond-related frameworks $[N(CH_3)_4][CuZn(CN)_4]$ and Cu[$4, 4', 4'', 4'''$-tetracyanotetraphenylmethane]$BF_4.xC_6H_5NO_2$. *J. Am. Chem. Soc.* **112**, 1546–1554 (1990).

21. Li, H., Eddaoudi, M., O'Keeffe, M. & Yaghi, O. M. Design and synthesis of an exceptionally stable and highly porous metal-organic framework. *Nature* **402**, 276–279 (1999).

22. Robson, R. A net-based approach to coordination polymers. *J. Chem. Soc., Dalton Trans.* 3735–3744 (2000).

23. O'Keeffe, M. Design of MOFs and intellectual content in reticular chemistry: a personal view. *Chem. Soc. Rev.* **38**, 1215–1217 (2009).

24. Kitagawa, S., Kitaura, R. & Noro, S.-I. Functional porous coordination polymers. *Angew. Chem. Int. Ed.* **43**, 2334–2375 (2004).

25. Li, W. *et al.* Chemically diverse and multifunctional hybrid organic–inorganic perovskites. *Nat. Rev. Mater.* **2**, 16099 (2017).

26. Morris, R. E. & Bu, X. Induction of chiral porous solids containing only achiral building blocks. *Nat. Chem.* **2**, 353–361 (2010).

27. Evans, J. D. & Coudert, F.-X. Microscopic mechanism of chiral induction in a metal–organic framework. *J. Am. Chem. Soc.* **138**, 6131–6134 (2016).

28. Paredes-García, V. *et al.* Crystal structure and magnetic properties of a new chiral manganese(II) three-dimensional framework: $Na_3[Mn_3(HCOO)_9]$. *Inorg. Chem.* **48**, 4737–4742 (2009).

29. Aston, J. C. & Saines, P. J. Transition-metal dependent cation disorder in the chiral cubic $AB(HCO_2)_3$ metal-organic frameworks (A = Li or Na, B = Mn or Co). *Z. Anorg. Allg. Chem.* **643**, 287–293 (2017).

30. Eikeland, E. *et al.* Alkali metal ion templated transition metal formate framework materials: Synthesis, crystal structures, ion migration, and magnetism. *Inorg. Chem.* **53**, 10178–10188 (2014).

31. Kawamichi, T., Haneda, T., Kawano, M. & Fujita, M. X-ray observation of a transient hemiaminal trapped in a porous network. *Nature* **461**, 633–635 (2009).

32. Inokuma, Y. *et al.* X-ray analysis on the nanogram to microgram scale using porous complexes. *Nature* **495**, 461–466 (2013).

33. Jain, P., Dalal, N. S., Toby, B. H., Kroto, H. W. & Cheetham, A. K. Order–disorder antiferroelectric phase transition in a hybrid inorganic–organic framework with the perovskite architecture. *J. Am. Chem. Soc.* **130**, 10450–10451 (2008).

34. Besara, T. *et al.* Mechanism of the order–disorder phase transition, and glassy behavior in the metal–organic framework $[(CH_3)_2NH_2]Zn(HCOO)_3$. *Proc. Natl. Acad. Sci., U.S.A.* **108**, 6828–6832 (2011).

35. Šimenas, M., Balčiūnas, S., Mączka, M., Banys, J. & Tornau, E. E. Structural phase transition in perovskite metal-formate frameworks: a Potts-type model with dipolar interactions. *Phys. Chem. Chem. Phys.* **18**, 18528 (2016).

36. Šimenas, M., Balčiūnas, S., Mączka, M., Banys, J. & Tornau, E. E. Exploring the antipolar nature of methylammonium lead halides: a Monte Carlo and pyrocurrent study. *J. Phys. Chem. Lett.* **8**, 4906–4911 (2017).

37. Tan, L. Z., Zheng, F. & Rappe, A. M. Intermolecular interactions in hybrid perovskites understood from a combined density functional theory and effective Hamiltonian approach. *ACS Energy Lett.* **2**, 937–942 (2017).

38. Simonov, A. & Goodwin, A. L. Designing disorder into crystalline materials. *arXiv:* 1912.00366 (2019).

39. Coates, C. S. *et al.* Ferroic multipolar order and disorder in cyanoelpasolite molecular perovskites. *Phil. Trans. R. Soc. Lond. A* **377**, 20180219 (2019).

40. Bak, P. & Jensen, M. H. Theory of helical magnetic structures and phase transitions in MnSi and FeGe. *J Phys. C: Solid State Phys.* **13**, L881 (1980).

41. Yu, X. Z. *et al.* Real-space observation of a two-dimensional skyrmion crystal. *Nature* **465**, 901–904 (2010).

42. Burhandt, S. & Fritz, L. Skyrmion lattice phase in three-dimensional chiral magnets from Monte Carlo simulations. *Phys. Rev. B* **88**, 195137 (2013).

43. Chen, J. *et al.* Helical and skyrmion lattice phases in three-dimensional chiral magnets: Effect of anisotropic interactions. *Sci. Rep.* **7**, 7392 (2017).

44. Karube, K. *et al.* Disordered skyrmion phase stabilized by magnetic frustration in a chiral magnet. *Sci. Adv.* **4**, eaar7043 (2018).

45. Du, Z.-Y. *et al.* Structural transition in the perovskite-like bimetallic azido coordination polymers $(NMe_4)_2[B'\cdot B''(N_3)_6]$ (B' = Cr^{3+}, Fe^{3+}; B'' = Na^+, K^+). *Cryst. Growth Des.* **14**, 3903–3909 (2014).

46. Evans, N. L. *et al.* Control of multipolar and orbital order in perovskite-like $[C(NH_2)_3]Cu_xCd_{1-x}(HCOO)_3$ metal–organic frameworks. *J. Am. Chem. Soc.* **138**, 9393–9396 (2016).

47. Côté, A. P. *et al.* Porous, crystalline, covalent organic frameworks. *Science* **310**, 1166–1170 (2005).

48. Weckhuysen, B. M. & Yu, J. Recent advances in zeolite chemistry and catalysis. *Chem. Soc. Rev.* **44**, 7022–7024 (2015).

49. Li, J., Corma, A. & Yu, J. Synthesis of new zeolite structures. *Chem. Soc. Rev.* **44**, 7112–7127 (2015).

50. Hicks, C. W. *et al.* Strong increase of T_c of Sr_2RuO_4 under both tensile and compressive strain. *Science* **344**, 283–285 (2014).

51. Cao, J. & Wu, J. Strain effects in low-dimensional transition metal oxides. *Mater. Sci. Eng. R* **71**, 35–52 (2011).

52. Palmer, B. A. *et al.* X-ray birefringence imaging. *Science* **344**, 1013–1016 (2014).

53. Zhou, Y. *et al.* Spatially resolved mapping of phase transitions in liquid-crystalline materials by X-ray birefringence imaging. *Chem. Sci.* **10**, 3005–3011 (2019).

54. Kikuchi, H., Yokota, M., Hisakado, Y., Yang, H. & Kajiyama, T. Polymer-stabilized liquid crystal blue phases. *Nat. Mater.* **1**, 64–68 (2002).

55. Wilson, M. N. *et al.* Extended elliptic skyrmion gratings in epitaxial MnSi thin films. *Phys. Rev. B* **86**, 144420 (2012).

56. Wilson, M. N., Butenko, A. B., Bogdanov, A. N. & Monchesky, T. L. Chiral skyrmions in cubic helimagnetic films: The role of uniaxial anisotropy. *Phys. Rev. B* **89**, 094411 (2014).

57. Metropolis, N. & Ulam, S. The Monte Carlo method. *J. Am. Stat. Assoc.* **44**, 335–341 (1949).

58. Schmidt, E. M. & Neder, R. B. Diffuse single-crystal scattering corrected for molecular form factor effects. *Acta Cryst. A* **73**, 231–237 (2017).

59. Dovesi, R. *et al.* CRYSTAL: a computational tool for the *ab initio* study of the electronic properties of crystals. *Z. Kristallogr.* **220**, 571–573 (2005).

60. Perdew, J. P., Burke, K. & Ernzerhof, M. Generalized gradient approximation made simple. *Phys. Rev. Lett.* **77**, 3865–3868 (1996).

61. Hutter, J., Iannuzzi, M., Schiffmann, F. & VandeVondele, J. CP2K: atomistic simulations of condensed matter systems. *WIREs Comput. Mol. Sci.* **4**, 15–25 (2014).

Acknowledgements A.L.G. thanks the European Research Council for funding (Advanced Grant 788144), and P. G. Welch (Oxford) and K. Gill (Manchester) for useful discussions. F.-X.C. acknowledge financial support from Agence Nationale de la Recherche under project "MATAREB" (ANR-18-CE29-0009-01) and access to high-performance computing platforms provided by GENCI grant A0070807069.

Author Contributions Statements E. H. W. carried out and analysed the Monte Carlo simulations. E.H.W. and F.-X.C. carried out and analysed the DFT calculations and AIMD simulations. A.L.G. conceived, designed and supervised the study. E.H.W. and A.L.G. wrote the paper with input from F.-X.C.

Competing Interests The authors declare that they have no competing financial interests.

Correspondence Correspondence and requests for materials should be addressed to A.L.G. (email: andrew.goodwin@chem.ox.ac.uk).